First-principles equation-of-state table of deuterium for inertial confinement fusion applications

S. X. Hu (□□□), B. Militzer, V. N. Goncharov, and S. Skupsky

Phys. Rev. B **84**, 224109 — Published 16 December 2011

DOI: 10.1103/PhysRevB.84.224109

FPEOS: A First-Principles Equation-of-State Table of Deuterium for Inertial Confinement Fusion Applications

S. X. Hu(胡素兴)[1,*], B. Militzer[2], V. N. Goncharov[1], and S. Skupsky[1]

[1]Laboratory for Laser Energetics, University of Rochester

250 E. River Road, Rochester, NY 14623

[2]Department of Earth and Planetary Science and Department of Astronomy

University of California, Berkeley, CA 94720

Understanding and designing inertial confinement fusion (ICF) implosions through radiation–hydrodynamics simulations rely on the accurate knowledge of the equation of state (EOS) of the deuterium and tritium fuels. To minimize the drive energy for ignition, the imploding shell of DT fuel must be kept as cold as possible. Such low-adiabat ICF implosions can access to coupled and degenerate plasma conditions, in which the analytical EOS models become inaccurate due to many-body effects. Using the path-integral Monte Carlo (PIMC) simulations we have derived a first-principles EOS (FPEOS) table of deuterium that covers typical ICF fuel conditions at densities ranging from 0.002 to 1596 g/cm^3 and temperatures of 1.35 eV to 5.5 keV. We report the internal energy and the pressure, and discuss the structure of the plasma in terms of pair-correlation functions. When compared with the widely used *SESAME* table and the revised *Kerley03* table, discrepancies in the internal energy and in the pressure are identified for moderately coupled and degenerate plasma conditions. In contrast to the

SESAME table, the revised *Kerley03* table is in better agreement with our FPEOS results over a wide range of densities and temperatures. Although subtle differences still exist for lower temperatures ($T < 10$ eV) and moderate densities (1 to 10 g/cm^3), hydrodynamics simulations of cryogenic ICF implosions using the FPEOS table and the *Kerley03* table have resulted in similar results for the peak density, areal density (ρR), and neutron yield, which are significantly different from the *SESAME* simulations.

PACS numbers: 52.25.Kn, 51.30.+i, 62.50.-p, 64.10.+h

I. INTRODUCTION

Inertial confinement fusion (ICF) has been pursued for decades since the concept was introduced in 1972 [1]. In the traditional central-hot-spot ignition designs, a capsule of cryogenic deuterium–tritium (DT) covered with plastic ablator is driven to implode either directly by intense laser pulses [2] or indirectly by x rays in a hohlraum [3]. To minimize the driving energy required for ignition, the imploding DT capsule should be maintained as cold as possible [4] for high compressions (larger than a 1000× that of the solid DT density) at the stagnation stage. This can either be done with fine-tuned shocks [5] or with ramp compression waves. The reduction in temperature leads to pressures in the imploding DT shell that are just above the Fermi degeneracy pressure (P_F). This is conventionally characterized by the so-called *adiabat* parameter $\alpha = P/P_F$. Low-adiabat ICF designs with $1 < \alpha < 2$ are currently studied with indirect-drive implosions at the National Ignition Facility (NIF) [6]. Direct-drive–ignition designs [5] for the NIF also place the DT-shell adiabat at a low value of $2 < \alpha < 3$. Cryogenic-DT targets scaled from

the hydro-equivalent NIF designs are routinely imploded with a direct drive at the Omega Laser Facility [7].

Since the compressibility of a material is determined by its equation of state (EOS) [8], the accurate knowledge of the EOS of the DT fuel is essential for designing ICF ignition targets and predicting the performance of the target during ICF implosions. To perform radiation–hydrodynamics simulations of ICF implosions, one needs to know the pressure and energy of the DT fuel and the ablator materials at various density and temperature conditions, which are usually provided by EOS tables or analytical formulas. Various EOS tables for deuterium have been assembled because its importance in ICF applications, planetary science and high-pressure physics.

The widely used *SESAME* EOS table of deuterium [9,10] was based on a *chemical model* for hydrogen [11–14] that describes the material in terms of well-defined chemical species like H_2 molecules, H atoms, and free protons and electrons. Their interaction as well as many-body and degeneracy effects are treated approximately. For the *SESAME* table, liquid perturbation theory was adopted in the molecular/atomic fluid phase for ICF plasma conditions. A first-order expansion that only takes into account nearest-neighbor interactions was used in the original *SESAME* table [9].

Chemical models are expected to work well in the regime of weak coupling. However, in ICF implosions, the DT shell goes through a wide range of densities from 0.1 up to 1000 g/cm^3 and temperatures varying from a few electron volts (eV) to several hundred electron volts [2,3], which include plasma conditions with moderately strong coupling. This provides the primary motivation for this paper, where we derive the deuterium from first-principles path-integral Monte Carlo simulations [15–18].

The conditions for a low-adiabat ($\alpha \approx 2.5$) cryogenic-DT implosion on OMEGA are shown in Figs. 1(a)–1(c). Figures 1(d)–1(f) characterize the conditions for a direct-drive–ignition design for NIF that is hydro-equivalent to the OMEGA implosion. In panels 1(a) and 1(d), we plot the laser pulse shapes. Panels 1(b) and 1(e) show the density (ρ) and temperature (T) path of the driven DT shell that we derived with one-dimensional (1-D) hydro simulations using the hydrocode *LILAC* [19]. The DT shell is predicted to undergo a variety of drive stages including several shocks and the final push by the main pulse.

The ρ–T path of the imploding DT shell can be projected onto a plane spanned by the coupling parameter $\Gamma = 1/(r_s k_b T)$ and the degeneracy parameter $\theta = T/T_F$. $T_F = (\hbar^2/2m_e k_b) \times (3\pi^2 n)^{2/3}$ is the Fermi temperature of the electrons in a fully ionized plasma and r_s is the Wigner–Seitz radius that is related to the number density of the electrons, $n = 3/\left(4\pi r_s^3\right)$. One finds in Figs. 1(c) and 1(f) that the imploding shells indeed pass through the strongly coupled ($\Gamma > 1$) and degenerate ($\theta < 1$) regimes and one expects coupling and degeneracy effects to play significant roles in the compression and yield production in low-adiabat ICF implosions [20].

Strong-coupling and degeneracy effects in ICF plasmas have recently attracted much attention since they may redefine the so-called 1-D physics of ICF implosions. The essential pieces of physics models used in ICF hydro simulations, such as the electron–ion energy relaxation rate [21], the thermal conductivity [22], the fusion-reaction rate [23], and viscosity and mutual diffusion in deuterium–tritium mixtures [24] in coupled and degenerated plasmas have been re-examined recently with experimental and

theoretical methods. EOS measurements of liquid deuterium along the principal Hugoniot reaching about 100 to 200 GPa have been performed using laser-driven shock waves [25–30], magnetically driven flyers [31,32], and convergent explosives [33,34]. First-principles computer simulations have emerged as the preferred theoretical tool to derive the EOS of deuterium under such extreme conditions. Two methods have been most successful: density-functional theory molecular dynamics (DFT-MD) [35–41] and the path-integral Monte Carlo (PIMC) [15–18]. In contrast to chemical models, these first-principles methods can take many-body effects fully into account. Results from such simulations have also been used to revise the original *SESAME* EOS table of deuterium to yield the improved *Kerley03* EOS table [10].

For ICF applications, we are especially concerned about the EOS accuracy along the implosion path in the density–temperature plane, i.e., in the range of ρ = 0.1 to 1000 g/cm^3 and T = 1 to 1000 eV. For such high temperatures, standard DFT methods become prohibitively expansive owing to the large number of electronic orbitals that would need to be included in the calculation to account for electronic excitations [42]. Orbital-free semi-classical simulation methods based on the Thomas–Fermi theory [43] are more efficient but they approximate electronic correlation effects and cannot represent chemical bonds. Therefore, in current form, they cannot describe the systems at lower temperatures accurately.

Path-integral Monte Carlo has been shown to work rather well for EOS calculations of low-Z materials such as deuterium [20,44] and helium [45,46]. In this paper we present a first-principles equation-of-state (FPEOS) table of deuterium from restricted PIMC simulations [47]. This method has been successfully applied to compute

the deuterium EOS [17,44] up to a density of $\rho = 5.388$ g/cm^3. At lower temperatures, the PIMC results have been shown to agree well with DFT-MD calculations for hydrogen [18] and more recently for helium [46].

Our FPEOS table derived from PIMC covers all of the DT-shell plasma conditions throughout the low-adiabat ICF implosions. Specifically, our table covers densities ranging from 0.002 to 1596 g/cm^3 and temperatures from 1.35 eV to 5.5 keV. When compared with the widely used *SESAME* EOS table and the revised *Kerley03* EOS table, discrepancies in the internal energy and in the pressure have been identified in moderately coupled and degenerate regimes. Hydrodynamics simulations for cryogenic ICF implosions using our FPEOS table and the *Kerley03* EOS table have resulted in similar peak density, areal density (ρR), and neutron yield, which differ significantly from the *SESAME* simulations.

This paper is organized as follows: A brief description of the path-integral Monte Carlo method is presented in Sec. II and the FPEOS table in Sec. III. In Sec. IV, we characterize the properties of the deuterium plasma for a variety of density and temperature conditions in terms of pair-correlation functions. Comparisons between the FPEOS table, the *SESAME* EOS, the *Kerley03* EOS, as well as the simple Debye–Hückel plasma model, are made in Sec. V. In Sec. VI, we analyze the implications of different EOS tables for ICF applications through hydro simulations and comparison with experiments. The paper is summarized in Sec. VII.

II. THE PATH-INTEGRAL MONTE CARLO METHOD

Path-integral Monte Carlo (PIMC) is the appropriate computational technique for simulating many-body quantum systems at finite temperatures. In PIMC calculations, electrons and ions are treated on equal footing as paths, which means the quantum effects of both species are included consistently, although for the temperatures under consideration, the zero-point motion and exchange effects of the nuclei are negligible.

The fundamental idea of the path-integral approach is that the density matrix of a quantum system at temperature T can be expressed as a convolution of density matrices at a much higher temperature, $M \times T$:

$$\rho(\mathbf{R},\mathbf{R}';\beta) = \int \mathrm{d}\mathbf{R}_1 \mathrm{d}\mathbf{R}_2 ... \mathrm{d}\mathbf{R}_{M-1}\, \rho(\mathbf{R},\mathbf{R}_1;\Delta\beta) \times \rho(\mathbf{R}_1,\mathbf{R}_2;\Delta\beta) ... \rho(\mathbf{R}_{M-1},\mathbf{R}';\Delta\beta). \tag{1}$$

This is an exact expression. The integral on the right can be interpreted as a weighted average over all *paths* that connect the points $\mathbf{R}$ and $\mathbf{R}'$. $\mathbf{R}$ is a collective variable that denote the positions of all particles $\mathbf{R} = \{\mathbf{r}_1, \ldots \mathbf{r}_N\}$. $\beta = 1/k_bT$ represents length of the path in "imaginary time" and $\Delta\beta = \beta/M$ is the size of each of the M time steps.

From the free-particle density matrix which can be used for the high-temperature density matrices,

$$\rho_0^{[1]}(\mathbf{r},\mathbf{r}';\beta) = \left(2\pi\hbar^2\beta/m\right)^{-d/2} \exp\left\{-\frac{(\mathbf{r}-\mathbf{r}')^2}{2\hbar\beta/m}\right\}, \tag{2}$$

one can estimate that the separation of two adjacent positions on the path, $\Delta r = \mathbf{r}_{i+1} - \mathbf{r}_i$ can only be on the order of $\sqrt{\hbar^2 \Delta\beta / m}$, while the separation of the two end points is approximately $\sqrt{\hbar^2 \beta / m}$. One can consequently interpret the positions $\mathbf{R}_1 \ldots \mathbf{R}_{M-1}$ as intermediate points on a path from **R** and **R′**. The multidimensional integration over all paths in Eq. (1) can be performed efficiently with Monte Carlo methods [47].

In general observables associated with operator $\hat{O}$ can be derived from

$$\left\langle \hat{O} \right\rangle = \frac{\int \mathrm{d}\mathbf{R} \int \mathrm{d}\mathbf{R}' \left\langle \mathbf{R} \middle| \hat{O} \middle| \mathbf{R}' \right\rangle \rho(\mathbf{R}', \mathbf{R}; \beta)}{\int \mathrm{d}\mathbf{R} \rho(\mathbf{R}, \mathbf{R}; \beta)}, \tag{3}$$

but for the kinetic and potential energies, E_K and E_P, as well as for pair-correlation functions only diagonal matrix elements (**R** = **R′**) are needed. The total internal energy follows from $E = E_K + E_P$ and the pressure P can be obtained from the virial theorem for Coulomb systems

$$P = \left(2E_K + E_P\right) / 3V. \tag{4}$$

V is the volume.

Electrons are fermions and their fermionic characters matters for the degenerate plasma conditions under consideration. This implies one needs to construct an antisymmetric many-body density matrix, which can be derived by introducing a sum of

all permutations $\mathcal{P}$ and then also include paths from $\mathbf{R}$ to $\mathcal{P}\mathbf{R}'$. While this approach works well for bosons [47], for fermions each permutation must be weighted by a factor $(-1)^{\mathcal{P}}$. The partial cancellation of contributions with opposite signs leads to an extremely inefficient algorithm when the combined position and permutation space is sampled directly. This is known as *Fermion sign problem*, and its severity increases as the plasma becomes more degenerate.

We deal with the Fermion sign problem by introducing the fixed node approximation [48,49]

$$\rho_{\mathrm{F}}(\mathbf{R},\mathbf{R}';\beta)=\frac{1}{N!}\sum_{\mathcal{P}}(-1)^{\mathcal{P}}\int\limits_{\substack{\mathbf{R}\to\mathcal{P}\mathbf{R}'\\ \rho_T(\mathbf{R},\mathbf{R}_t;t)>0}}\mathrm{d}\mathbf{R}_t\, e^{-S[\mathbf{R}_t]}, \tag{5}$$

where one only includes those paths that satisfy the nodal constraint, $\rho_T(\mathbf{R},\mathbf{R}_t;\, t) > 0$, at every point. $S[\mathbf{R}_t]$ is the action of the path and ρ_T is a fermionic trial density that must be given in analytic form. For this paper, we rely on free-particle nodes,

$$\rho_T(\mathbf{R},\mathbf{R}';\beta)=\begin{vmatrix}\rho^{[1]}(\mathbf{r}_1,\mathbf{r}_1';\beta)\ldots\rho^{[1]}(\mathbf{r}_N,\mathbf{r}_1';\beta)\\ \\ \rho^{[1]}(\mathbf{r}_1,\mathbf{r}_N';\beta)\ldots\rho^{[1]}(\mathbf{r}_N,\mathbf{r}_N';\beta)\end{vmatrix}. \tag{6}$$

but the nodes of a variational-density matrix [50] have also been employed in PIMC computations [17,45,46].

We have performed a number of convergence tests to minimize errors from using a finite time step and from a finite number of particles in cubic simulation cells with periodic boundary conditions. We determined a time step of $\Delta\beta \leq [100 \times k_b T_F]^{-1}$ was sufficient to accurately account for all interactions and degeneracy effects. We perform our PIMC calculations with different numbers of atoms depending on the deuterium density: $N = 64$ atoms for $\rho < 2.5$ g/cm^3, $N = 128$ atoms for $2.5 < \rho < 10.5$ g/cm^3, and $N = 256$ atoms for $\rho > 10.5$ g/cm^3. For each of these density ranges, our convergence tests on the number of atoms in box showed that the box-size typically needs to be at least several (≥3) times larger than the plasma Debye length to guarantee reliable results.

III. THE FPEOS TABLE OF DEUTERIUM

We have carried out PIMC calculations for a variety of density and temperature conditions that are of interest to inertial confinement fusion applications. The resulting FPEOS table for deuterium covers the density range from 0.0019636 g/cm^3 (r_s = 14 Bohr) to 1596.48802 g/cm^3 (r_s = 0.15 Bohr) and the temperature interval from 15,625 K (≈1.35 eV) to 6.4×10^7 K (≈5515.09 eV). Figure 2 shows the conditions for every simulation. The lines for $\Gamma = 1$ and $\theta = 1$ indicate the boundaries between coupled/uncoupled and degenerate/non-degenerate plasma conditions. Plasma conditions in the upper left corner of the diagram are weakly coupled and classical $(\Gamma \ll 1 \text{ and } \theta \gg 1)$, while the lower right of the diagram represent strongly coupled and highly degenerate conditions $(\Gamma \gg 1 \text{ and } \theta \ll 1)$. The lowest temperatures in our PIMC calculations reached the regime of $\theta \approx 0.1$. For temperatures higher than 5.5-keV,

deuterium plasmas become weakly-coupled in the density range we explored; and their EOS can be analytically obtained from the Debye-Hückel model as we discuss below.

To give an example for the ICF plasma conditions, we added the conditions of an imploding DT capsule shown in Fig. 1 to Fig. 2. It can be seen that the DT shell undergoes a change from a strongly coupled to an uncoupled regime during the shock transits. Accordingly, the electronic conditions change from fully degenerated to partially degenerate.

All these conditions are covered by our PIMC results that we have assembled into the following FPEOS Table I. The pressure and the internal energy as well as their statistical error bars from PIMC simulations are listed for different density and temperature conditions.

IV. PARTICLE CORRELATIONS

The correlation functions $g(r)$ between different pairs of particles such as electron–electron, electron–ion, and ion–ion are particularly interesting for analyzing the physical and chemical changes in the plasma at various density and temperature conditions. The $g(r)$ are available directly in PIMC simulations. We first show the density effects on the structure of the fluid by showing how the $g(r)$ functions change with density for the three temperatures of 15,625 K, 2.5×10^5 K, and 2×10^6 K in Figs. 3–5.

Figure 3(a) shows a clear peak in the ion–ion correlation function $g_{dd}(r)$ for 0.1 g/cm^3 at the molecular bond length of 1.4 Bohr. As the density of deuterium increases to 1.0 g/cm^3, one observes a drastic reduction in peak height, which demonstrates the pressure-induced dissociation of D_2 molecules, confirming earlier PIMC results [44,51].

This interpretation is also supported by the reduction of peak at $r = 0$ in the $g_{de}(r)$ function in Fig. 3(b). Furthermore, the positive correlation between pair of electrons with antiparallel spin in Fig. 3(d) disappears with increasing density since they are no longer bound into molecules. Figure 3(c) shows that there is always a strong repulsion between electrons with parallel spins because of the Pauli exclusion principle but they approach each other more at higher densities.

Figures 4 and 5 show the pair-correlation functions for different densities at much higher temperatures of 2.5×10^5 K and 2×10^6 K. At these temperatures, D_2 molecules have completely dissociated as indicated by the absence of the peak in the ion–ion correlation function. The attractive forces between pair of ions have disappeared and repulsion now dominates their interactions. At higher densities, particles are "packed" more tightly and approach each other significantly more so that the $g(r)$ rise more steeply and reach the values of 0.5 at much smaller distances.

In Fig. 6, we compare the pair-correlation functions for the fixed density of 10 g/cm^3 for temperatures ranging from 1.25×10^5 K to 2×10^6 K. It is interesting to note there is relatively little variation between the three curves below the Fermi temperature of $T_F = 8.8 \times 10^5$ K but they differ significantly at 2×10^6 K. This is a manifestation of Fermi-degeneracy effects in which the electrons approach the ground state for temperatures well below the Fermi temperature. Then much of the temperature dependence of the pair-correlation functions disappears. For example, the pair-correlation functions of electrons with antiparallel spins are almost identical for the two lowest temperatures of 1.25×10^5 K and 2.5×10^5 K, but they differ substantially from results at well above T_F. When the temperature rises above T_F, Pauli exclusion effects are reduced,

the electrons start to occupy a variety of states, which then has a positive feedback on the mobility of the ions.

V. COMPARISONS OF THE FPEOS TABLE WITH *SESAME* AND *KERLEY03* MODELS

In this section, we compare the pressures and internal energies in our FPEOS table with predictions from the well-known semi-analytical *SESAME* and *Kerley03* EOS tables. To illustrate how much the system deviates from an ideal plasma, we have normalized both pressure and energy to their corresponding values (E_{id} and P_{id}) of non-interacting gas of classical ions and fermionic electrons. This removes most of the temperature dependence and emphasizes the effects of the Coulomb interaction, which leads to a reduction in pressure and energy below the non-interacting values in all cases.

In Figs. 7–9, we plot the pressure and the internal energy as a function of density for different temperatures ranging from 31,250 to 4×10^6 K. Figures 10–13 show them as function of temperature for different densities varying between 0.1 and 84.19 g/cm^3.

In Fig. 7, we compare FPEOS, *SESAME*, and *Kerley03* results at a comparatively low temperature of 31,250 K. This is difficult regime to describe by chemical models because the plasma consists of neutral species like molecules and atoms, as well as charged particles such as ions and free electrons. The interaction between neutral and charged species is very difficult analytically while it poses no major challenge to first-principles simulations. As shown in Fig. 7(a), the *SESAME* EOS predicts overall higher pressures at low density ($\rho \leq 0.3$ g/cm^3) but then all three models agree with each other at higher densities. The improved *Kerley03* table still showed some discrepancy at very low

densities, even though some improvements to the ionization equilibrium model have been made [10].

Figure 7(b) shows that the internal energies predicted by *SESAME* and *Kerley03* are overall lower than the FPEOS values. The higher the density, the more discrepancy. Again, this manifests the difficulty of chemical models at such plasma conditions.

One expects the pressure and internal energy to approach the values of a non-interacting gas in the low-density and the high-density limit. At low density, particles are so far away from each other that the interaction effects become negligible. At high density, Pauli exclusion effects dominate over all other interactions and all thermodynamic function can be obtained from the ideal Fermi gas. Only at an intermediate density range which still spans several orders of magnitude does the Coulomb interaction matter and significant deviations for the ideal behavior is observed.

For a higher temperature of 2.5×10^5 K, the pressure and energy are compared in Fig. 8. The low-density deuterium at this temperature becomes fully ionized and can therefore be described by the Debye–Hückel plasma model [52], which is based on the self-consistent solution of the Poisson equation for a system of screened charges. The pressure and energy per particle (counting electrons and ions) can be explicitly expressed as

$$P_{\mathrm{D}} = P_{\mathrm{id}} - \frac{k_b T}{24\pi\lambda_{\mathrm{D}}^3} \text{ and } E_{\mathrm{D}} = E_{\mathrm{id}} - \frac{k_b T}{8\pi n\lambda_{\mathrm{D}}^3}, \tag{7}$$

with the particle number density n, the Boltzmann constant k_b, and the Debye length $\lambda_{\mathrm{D}} = \sqrt{k_b T / 4\pi n e^2}$.

We have added the Debye–Hückel results to Figs. 8–13. In Fig. 8 one finds that the simple Debye–Hückel model agrees perfectly with our PIMC calculations in the lower densities up to 0.1 g/cm^3, where the improved *Kerley03* EOS also gives very similar pressures and energies. On the other hand, the *SESAME* EOS overestimates both pressure and energy even at such low densities.

Figure 8(a) exposes an artificial cusp in pressure in *Kerley03* EOS at densities of 1.5 to 4 g/cm^3, while the internal-energy curve is smooth. This artificial pressure cusp appears for all temperatures at roughly the same density and may be related to the artificial double compression peaks in the principal Hugoniot predicted by *Kerley03* EOS [10]. The Debye–Hückel model fails at densities higher than 0.2 g/cm^3 for this temperature. It is only applicable to weakly interacting plasmas but otherwise predicts unphysically low pressures and energies.

Figure 9 shows that as the temperature increased to 4×10^6 K, the Debye–Hückel model agrees very well with FPEOS in both pressure and energy over a wide range of densities up to 20 g/cm^3. Significant differences in both pressure and energy are again found for the *SESAME* EOS, when compared to FPEOS and *Kerley03* tables. It should also be noted that the internal energy predicted by *Kerley03* is slightly lower than those of FPEOS and the Debye–Hückel model for $\rho = 0.1$ to 20 g/cm^3.

In Figs. 10–13, we compare the pressure and energy versus temperature for specific densities of 0.1, 1.0, 10.0, and 84.19 g/cm^3. At high temperatures where the plasma is fully ionized, the Debye–Hückel model reproduces the FPEOS pressures and

energies very well. It is interesting to note that the *SESAME* table overestimates the pressure and energy even for a fully ionized plasma at densities greater than 1.0 g/cm^3 as shown in Figs. 11–13. For the very low density of 0.1 g/cm^3, Fig. 10 shows that the improved *Kerley03* agrees very well with FPEOS, while the *SESAME* results are noticeably higher. Moreover, the improvements made to *Kerley03* have resulted in a remarkable agreement with FPEOS for intermediate densities of 0.1 and 10.0 g/cm^3 depicted by Figs. 11 and 12. Only a small deviation in the internal energy between *Kerley03* and our FPEOS results can be found at the lowest temperature for 1.0 g/cm^3.

At a higher density of 84.19 g/cm^3, the *SESAME* EOS again significantly deviates from both the FPEOS and the *Kerley03* EOS, as is illustrated in Fig. 13. The latter two EOS tables give very similar results in internal energy for almost the entire temperature range, although the pressures predicted by *Kerley03* are higher than the FPEOS ones for temperatures varying from 2×10^6 K to 2×10^7 K. In contrast to the significant EOS differences seen in *SESAME*, the improved *Kerley03* table is overall in better agreement with the FPEOS table, although subtle discrepancies and an artificial pressure cusp still exist in the *Kerley03* EOS.

VI. APPLICATIONS TO ICF

With the EOS comparisons discussed above, we now investigate what differences can be observed when these EOS tables are applied to simulating ICF shock-timing experiments and target implosions. Using radiation–hydrodynamics codes (both one-dimensional *LILAC* [19] and two-dimensional *DRACO* [53]) for simulations of

experiments, we can explore the implications of our first-principles equation-of-state table for the understanding and designing of ICF targets.

We first study the shock-timing experiments [54,55] performed at the Omega Laser Facility. As the fuel entropy in ICF implosions is set by a sequence of shocks, the timing of shock waves in liquid deuterium is extremely important for the ICF target performance. In shock-timing experiments, 900-μm-diam, 10-μm-thick carbon deuterium (CD) spherical shells in a cone-in-shell geometry [54] were filled with liquid deuterium. VISAR (velocity interferometry system for any reflector) was used to measure the shock velocity. As shown in Fig. 14(a), the triple-picket laser pulses are designed to launch three shocks into the liquid deuterium. The experimental results are plotted in Fig. 14(b), in which the shock-front velocity is shown as a function of time. One finds that when the second shock catches up to the first one at ~1.5 ns, the shock-front velocity exhibits a sudden jump. Another velocity jump at 2.2 ns occurs when the third strong shock overtakes the previous two. With the hydrocode *LILAC*, we have simulated the shock-timing experiments using different EOS tables including FPEOS, *SESAME*, *Kerley03*, and QEOS [56]. The radiation–hydrodynamic simulations have used the standard flux-limited (f = 0.06) thermal transport model, although a nonlocal model has resulted in better agreement with experiment for the speed of first shock [55]. The results of FPEOS, *SESAME*, and *Kerley03* are in good agreement with the experimental observation, while the QEOS predicts much lower shock velocity and early catching up time. The shock-timing experiments can only explore a small range of deuterium densities (0.6 to 2.5 g/cm^3) and temperatures (3 to 10 eV). In these plasma conditions, *SESAME* and *Kerley03* have been adjusted [10] to match to the first-principles calculations, which can

be seen in Fig. 11. Therefore, the shock-velocity differences predicted by the FPEOS, *SESAME*, and *Kerley03* are very small in such plasma conditions.

Next, we examine the implications of coupling and degeneracy effects in ICF implosions. The possible differences in target compression and fusion yields of ICF implosions are investigated through radiation–hydrodynamic simulations using FPEOS in comparison to results predicted by *SESAME* and *Kerley03*. The *LILAC* simulation results are compared in Figs. 15 and 16, respectively, for a DT implosion on OMEGA and a hydro-equivalent direct-drive design on the NIF. In Figs. 15(a) and 16(a), we plot the laser pulse shapes consisting of triple pickets and the step main pulse. The cryogenic OMEGA DT target (860-μm diameter) has a 10-μm deuterated plastic ablator and ~65 μm of DT ice. Figure 15(b) shows the density and temperature profiles at the end of the laser pulse (t = 3.8 ns) from the FPEOS (red solid line), the *SESAME* (green dashed line), and the *Kerley03* (blue dashed–dotted line) simulations. At this time, the shell has converged to a radius of ~160 μm from its original radius of ~430 μm. The shell's peak density and average temperature were $\rho \approx 5.6$ g/cm^3 and $T \approx 21$ eV, which correspond to the coupled and degenerate regimes with $\Gamma \approx 1.22$ and $\theta \approx 0.47$. It is shown that the FPEOS simulation predicted ~10%-lower peak density but ~15%-higher temperature relative to the *SESAME* prediction. As shown by the comparisons made in Fig. 8 and Ref. 20, the FPEOS predicts slightly stiffer deuterium than *SESAME* at a similar temperature regime. This explains the lower peak density seen in Fig. 15(b). The ~15%-higher temperature in the FPEOS case was originated from the lower internal energy [see Fig. 8(b)]. Since the laser ablation does the same work/energy to the shell compression and its kinetic motion, a lower internal energy in FPEOS means more energy is

partitioned to heat the shell, thereby resulting in a higher temperature. Such a temperature increase and density drop can have consequences in the implosion performance. Despite the subtle EOS differences discussed above, the *Kerley03* simulation shows very similar results when compared to FPEOS. Only small differences in the temperature profile can be seen between the FPEOS and *Kerley03* simulations, both of which are in remarkable contrast to the *SESAME* case. Figure 15(c) shows the density profile at peak compression, in which the predicted peak density ($\rho_p \approx 210$ g/cm^3) is ~25% lower according to FPEOS and *Kerley03* compared to the *SESAME* prediction ($\rho_p \approx 260$ g/cm^3). The history of areal-density (ρR) evolution and neutron production are shown in Fig. 15(d). One sees that the peak ρR and neutron yield are also reduced by ~10% to 20% when the FPEOS and *Kerley03* are compared to the *SESAME* prediction. The absolute neutron yield drops from ~8.44×10^{13} predicted by *SESAME* to ~6.91×10^{13} (FPEOS) and ~6.93×10^{13} (*Kerley03*).

Figure 16 shows the similar effects for the hydro-equivalent, direct-drive NIF design with 1-MJ laser energy. The NIF target (ϕ = 2.954 mm) consists of a 27-μm plastic ablator and 170 μm of DT ice. The triple-picket drive pulse has a total duration of ~11.4 ns and a peak power of ~240 TW. We also found a decrease in ρ_p and a slight temperature increase for the FPEOS and *Kerley03* relative to *SESAME* simulations near the end of the laser pulse (t = 9.2 ns), shown in Fig. 16(b). The peak density at stagnation dropped from 481 (*SESAME*) to ~ 445 g/cm^3 (FPEOS/*Kerley03*), which is indicated by Fig. 16(c). The resulting ρR and neutron yield as a function of time are plotted in Fig. 16(d). The yield dropped from the *SESAME* value of $Y = 1.75 \times 10^{19}$ to $Y = 1.57 \times$

10^{19} (FPEOS) and $Y = 1.55 \times 10^{19}$ (*Kerley03*). Consequently, the energy gain decreased from 49.1 (*SESAME*) to 44.2 (FPEOS) and 43.8 (*Kerley03*). It is noted that the ~11% gain reduction for this design is more modest than the 1.5-MJ NIF design discussed in Ref. 20, in which more than ~20% gain difference was seen between FPEOS and *SESAME* simulations. This is attributed to the different density–temperature trajectories that the two designed implosions undergo, in which the EOS variations differ among FPEOS, *SESAME*, and *Kerley03*.

Finally, we discuss the implications of the coupling and degeneracy effects in FPEOS to ICF target performance beyond the 1-D physics studied above. Since we know that various perturbations seeded by target roughness and lasers can grow via the Rayleigh–Taylor (RT) instability [57] during the shell acceleration/deceleration phases in ICF implosions, it is important to properly simulate the RT growth of fusion fuel to understand target performance (compression and neutron yields) [58,59]. Since the RT growth depends on the compressibility of materials, the accurate equation of state of deuterium is essential to ICF designs. As an example, we have used our 2-D radiation–hydrodynamic code *DRACO* to simulate the cryogenic-DT implosion on OMEGA (discussed in Fig. 15). The various perturbation sources, including the target offset, ice roughness, and laser irradiation nonuniformities measured from experiments, have been taken into account up to a maximum mode of $\ell = 150$. We have compared the FPEOS and *SESAME* simulation results in Fig. 17 for $t = 3.85$ ns near the end of acceleration, in which the density contours are plotted in the z–r plane (azimuthal symmetry with respect to the z axis is assumed). Visible differences in the DT shell's density can be seen even

by eye from Figs. 17(a) and 17(b). The FPEOS simulation resulted in more "holes" and density modulations along the shell than the *SESAME* case.

To further analyze the perturbation amplitudes, we have decomposed the ablation-surface modulations into the modal spectrum [shown in Fig. 18(a)] at the start of shell acceleration (t = 3.0 ns). We find that the FPEOS predicted larger amplitudes than the *SESAME* case over almost the entire modal range. As the deuterium Hugoniot was shown in Ref. 20, the FPEOS predicted softer deuterium compared to *SESAME* for pressures below ~2 Mbar. Therefore, the softer deuterium can be more easily "imprinted" by the perturbations brought in via the series of shocks. This results in larger perturbation amplitudes in FPEOS than in *SESAME* simulations. The Rayleigh–Taylor instability further amplifies these perturbations during the shell acceleration. As indicated by Fig. 18(b), the $\sigma_{\rm rms}$ of fuel ρR modulation increased to a few mg/cm^2 at the end of the laser pulse. These perturbations penetrated into the inner surface of the DT shell will become the seeds for further RT growth during the shell's deceleration phase. They eventually distort the hot-spot temperature and density, thereby reducing the neutron production. At the end, we found that the *SESAME* simulation resulted in a neutron-averaged ion temperature of $\langle T_{\rm i}\rangle$ = 2.6 keV and a neutron yield of $Y = 5.2 \times 10^{12}$; while because of the predicted larger perturbations, the FPEOS simulation has given a $\langle T_{\rm i}\rangle$ = 2.3 keV and a neutron yield of $Y = 3.7 \times 10^{12}$, which is closer to the experimental observations of $\langle T_{\rm i}\rangle = 1.8 \pm 0.5$ keV and $Y = 1.9 \times 10^{12}$.

VII. SUMMARY

In conclusion, we have derived a first-principles equation-of-state table of deuterium for ICF applications from PIMC calculations. The derived FPEOS table covers the plasma density and temperature conditions in low-adiabat ICF implosions. In comparison with the chemical-model–based *SESAME* table, the FPEOS table shows a significant difference in internal energy and pressure for coupled and degenerate plasma conditions; while the recently improved *Kerley03* table exhibited fewer and smaller discrepancies when compared to the FPEOS predictions for temperatures higher than ~10 eV. Although subtle differences at lower temperatures (T < 10 eV) and moderate densities (1 to 10 g/cm^3) have been identified and an artificial pressure cusp still exists in the *Kerley03* table, radiation–hydrodynamics simulations of cryogenic ICF implosions using the FPEOS and *Kerley03* tables have given similar peak density, areal density (ρR), and neutron yield, which are remarkably different from the *SESAME* simulations. Both the FPEOS and the *Kerley03* predicted ~25% less peak density, ~10% smaller ρR, and ~10% to 20% less neutron yield, when compared to the *SESAME* case. Two-dimensional simulations further demonstrated the significant differences in target performance between the FPEOS and *SESAME* simulations. In general, the FPEOS simulations resulted in better agreement with experimental observations in terms of ion temperature and neutron yield. It is also noted that the extreme conditions covered by the FPEOS table are also important in astrophysics and planetary sciences, for example, to model the evolution of stars [60] and to understand the thermodynamical properties of stellar matter [61].

We have also noted that a multi-phase EOS of DT [62] has recently been built by combining the low-temperature points of DFT-MD simulations with our FPEOS table. It

has been shown that the multi-phase EOS simulations for direct-drive ICF target designs gave very similar results [63] when compared to our FPEOS simulations [20]. In addition, other *ab-initio* methods such as coupled electron-ion quantum Monte Carlo (CEIMC) have been used to benchmark the *SESAME* and *Kerley03* EOS tables in the low temperature and density regimes [64]. Finally, it is possible that some of transport properties of deuterium plasmas may be self-consistently derived from these PIMC simulations by indirectly using thermodynamic relationships. However, such methods have not been developed yet, and they can be a subject for future studies.

ACKNOWLEDGMENT

This work was supported by U.S. Department of Energy Office of Inertial Confinement Fusion under Cooperative Agreement No. DE-FC52-08NA28302, the University of Rochester, and New York State Energy Research and Development Authority. SXH would like to thank the support by the National Science Foundation under the NSF TeraGrid grant PHY110009. This work partially utilized the NICS' Kraken Supercomputer. BM acknowledges support from NSF and NASA.

REFERENCES

1. J. Nuckolls, L. Wood, A. Thiessen, and G. Zimmerman, Nature **239**, 139 (1972); S. Atzeni and J. Meyer-ter-Vehn, *The Physics of Inertial Fusion: Beam Plasma Interaction, Hydrodynamics, Hot Dense Matter*, International Series of Monographs on Physics (Clarendon Press, Oxford, 2004).

2. R. L. McCrory, D. D. Meyerhofer, R. Betti, R. S. Craxton, J. A. Delettrez, D. H. Edgell, V. Y. Glebov, V. N. Goncharov, D. R. Harding, D. W. Jacobs-Perkins, J. P. Knauer, F. J. Marshall, P. W. McKenty, P. B. Radha, S. P. Regan, T. C. Sangster, W. Seka, R. W. Short, S. Skupsky, V. A. Smalyuk, J. M. Soures, C. Stoeckl, B. Yaakobi, D. Shvarts, J. A. Frenje, C. K. Li, R. D. Petrasso, and F. H. Séguin, Phys. Plasmas **15**, 055503 (2008); D. D. Meyerhofer, R. L. McCrory, R. Betti, T. R. Boehly, D. T. Casey, T. J. B. Collins, R. S. Craxton, J. A. Delettrez, D. H. Edgell, R. Epstein, K. A. Fletcher, J. A. Frenje, Y. Y. Glebov, V. N. Goncharov, D. R. Harding, S. X. Hu, I. V. Igumenshchev, J. P. Knauer, C. K. Li, J. A. Marozas, F. J. Marshall, P. W. McKenty, P. M. Nilson, S. P. Padalino, R. D. Petrasso, P. B. Radha, S. P. Regan, T. C. Sangster, F. H. Séguin, W. Seka, R. W. Short, D. Shvarts, S. Skupsky, J. M. Soures, C. Stoeckl, W. Theobald, and B. Yaakobi, Nucl. Fusion **51**, 053010 (2011).

3. J. D. Lindl, Phys. Plasmas **2**, 3933 (1995).

4. R. Betti and C. Zhou, Phys. Plasmas **12**, 110702 (2005); R. Betti, K. Anderson, T. R. Boehly, T. J. B. Collins, R. S. Craxton, J. A. Delettrez, D. H. Edgell, R. Epstein, V. Y. Glebov, V. N. Goncharov, D. R. Harding, R. L. Keck, J. H. Kelly, J. P. Knauer, S. J. Loucks, J. A. Marozas, F. J. Marshall, A. V. Maximov, D. N. Maywar, R. L. McCrory, P. W. McKenty, D. D. Meyerhofer, J. Myatt, P. B. Radha, S. P. Regan, C. Ren, T. C. Sangster, W. Seka, S. Skupsky, A. A. Solodov, V. A. Smalyuk, J. M. Soures, C. Stoeckl, W. Theobald, B. Yaakobi, C. Zhou, J. D. Zuegel, J. A. Frenje, C. K. Li, R. D. Petrasso, and F. H. Séguin, Plasma Phys. Control. Fusion **48**, B153 (2006).

5. V. N. Goncharov, T. C. Sangster, T. R. Boehly, S. X. Hu, I. V. Igumenshchev, F. J. Marshall, R. L. McCrory, D. D. Meyerhofer, P. B. Radha, W. Seka, S. Skupsky, C. Stoeckl, D. T. Casey, J. A. Frenje, and R. D. Petrasso, Phys. Rev. Lett. **104**, 165001 (2010).

6. E. M. Campbell and W. J. Hogan, Plasma Phys. Control. Fusion **41**, B39 (1999).

7. T. R. Boehly, D. L. Brown, R. S. Craxton, R. L. Keck, J. P. Knauer, J. H. Kelly, T. J. Kessler, S. A. Kumpan, S. J. Loucks, S. A. Letzring, F. J. Marshall, R. L. McCrory, S. F. B. Morse, W. Seka, J. M. Soures, and C. P. Verdon, Opt. Commun. **133**, 495 (1997).

8. S. X. Hu, V. A. Smalyuk, V. N. Goncharov, J. P. Knauer, P. B. Radha, I. V. Igumenshchev, J. A. Marozas, C. Stoeckl, B. Yaakobi, D. Shvarts, T. C. Sangster, P. W. McKenty, D. D. Meyerhofer, S. Skupsky, and R. L. McCrory, Phys. Rev. Lett. **100**, 185003 (2008).

9. G. I. Kerley, Phys. Earth Planet. Inter. **6**, 78 (1972).

10. G. I. Kerley, Sandia National Laboratory, Albuquerque, NM, Report SAND2003-3613 (2003).

11. D. Saumon and G. Chabrier, Phys. Rev. A **46**, 2084 (1992).

12. M. Ross, Phys. Rev. B **58**, 669 (1998).

13. F. J. Rogers, Contrib. Plasma Phys. **41**, 179 (2001).

14. H. Juranek, R. Redmer, and Y. Rosenfeld, J. Chem. Phys. **117**, 1768 (2002).

15. C. Pierleoni, D. M. Ceperley, B. Bernu, and W. R. Magro, Phys. Rev. Lett. **73**, 2145 (1994).

16. W. R. Magro, D. M. Ceperley, C. Pierleoni, and B. Bernu, Phys. Rev. Lett. **76**, 1240 (1996).

17. B. Militzer and D. M. Ceperley, Phys. Rev. Lett. **85**, 1890 (2000).

18. B. Militzer, D. M. Ceperley, J. D. Kress, J. D. Johnson, L. A. Collins, and S. Mazevet, Phys. Rev. Lett. **87**, 275502 (2001).

19. J. Delettrez, R. Epstein, M. C. Richardson, P. A. Jaanimagi, and B. L. Henke, Phys. Rev. A **36**, 3926 (1987).

20. S. X. Hu, B. Militzer, V. N. Goncharov, and S. Skupsky, Phys. Rev. Lett. **104**, 235003 (2010).

21. M. S. Murillo and M. W. C. Dharma-wardana, Phys. Rev. Lett. **100**, 205005 (2008); B. Jeon, M. Foster, J. Colgan, G. Csanak, J. D. Kress, L. A. Collins, and N. Grønbech-Jensen, Phys. Rev. E **78**, 036403 (2008); G. Dimonte and J. Daligault, Phys. Rev. Lett. **101**, 135001 (2008); J. N. Glosli, F. R. Graziani, R. M. More, M. S. Murillo, F. H. Streitz, M. P. Surh, L. X. Benedict, S. Hau-Riege, A. B. Langdon, and R. A. London, Phys. Rev. E **78**, 025401 (R) (2008); L. X. Benedict, J. N. Glosli, D. F. Richards, F. H. Streitz, S. P. Hau-Riege, R. A. London, F. R. Graziani, M. S. Murillo, and J. F. Benage, Phys. Rev. Lett. **102**, 205004 (2009); B. Xu and S. X. Hu, Phys. Rev. E **84**, 016408 (2011).

22. V. Recoules, F. Lambert, A. Decoster, B. Canaud, and J. Clérouin, Phys. Rev. Lett. **102**, 075002 (2009).

23. E. L. Pollock and B. Militzer, Phys. Rev. Lett. **92**, 021101 (2004).

24. J. D. Kress, J. S. Cohen, D. A. Horner, F. Lambert, and L. A. Collins, Phys. Rev. E **82**, 036404 (2010).

25. L. B. Da Silva, P. Celliers, G. W. Collins, K. S. Budil, N. C. Holmes, T. W. Barbee, Jr., B. A. Hammel, J. D. Kilkenny, R. J. Wallace, M. Ross, R. Cauble, A. Ng, and G. Chiu, Phys. Rev. Lett. **78**, 483 (1997).

26. G. W. Collins, L. B. Da Silva, P. Celliers, D. M. Gold, M. E. Foord, R. J. Wallace, A. Ng, S. V. Weber, K. S. Budil, and R. Cauble, Science **281**, 1178 (1998).

27. G. W. Collins, P. Celliers, L. B. Da Silva, R. Cauble, D. Gold, M. Foord, K. S. Budil, R. Stewart, N. C. Holmes, M. Ross, B. A. Hammel, J. D. Kilkenny, R. J. Wallace, and A. Ng, Phys. Plasmas **5**, 1864 (1998).

28. A. N. Mostovych, Y. Chan, T. Lehecha, A. Schmitt, and J. D. Sethian, Phys. Rev. Lett. **85**, 3870 (2000); A. N. Mostovych, Y. Chan, T. Lehecha, L. Phillips, A. Schmitt, and J. D. Sethian, Phys. Plasmas **8**, 2281 (2001).

29. T. R. Boehly, D. G. Hicks, P. M. Celliers, T. J. B. Collins, R. Earley, J. H. Eggert, D. Jacobs-Perkins, S. J. Moon, E. Vianello, D. D. Meyerhofer, and G. W. Collins, Phys. Plasmas **11**, L49 (2004).

30. D. G. Hicks, T. R. Boehly, P. M. Celliers, J. H. Eggert, S. J. Moon, D. D. Meyerhofer, and G. W. Collins, Phys. Rev. B **79**, 014112 (2009).

31. M. D. Knudson, D. L. Hanson, J. E. Bailey, C. A. Hall, J. R. Asay, and W. W. Anderson, Phys. Rev. Lett. **87**, 225501 (2001); M. D. Knudson, D. L. Hanson, J. E. Bailey, C. A. Hall, and J. R. Asay, Phys. Rev. Lett. **90**, 035505 (2003).

32. M. D. Knudson, D. L. Hanson, J. E. Bailey, C. A. Hall, J. R. Asay, and C. Deeney, Phys. Rev. B **69**, 144209 (2004).

33. S. I. Belov, G. V. Boriskov, A. I. Bykov, R. I. Il'kaev, N. B. Luk'yanov, A. Y. Matveev, O. L. Mikhailova, V. D. Selemir, G. V. Simakov, R. F. Trunin, I. P. Trusov, V. D. Urlin, V. E. Fortov, and A. N. Shuikin, JETP Lett. **76**, 433 (2002).

34. V. E. Fortov, R. I. Ilkaev, V. A. Arinin, V. V. Burtzev, V. A. Golubev, I. L. Iosilevskiy, V. V. Khrustalev, A. L. Mikhailov, M. A. Mochalov, V. Y. Ternovoi, and M. V. Zhernokletov, Phys. Rev. Lett. **99**, 185001 (2007).

35. L. Collins, I. Kwon, J. Kress, N. Troullier, and D. Lynch, Phys. Rev. E **52**, 6202 (1995).

36. T. J. Lenosky, S. R. Bickham, J. D. Kress, and L. A. Collins, Phys. Rev. B **61**, 1 (2000).

37. G. Galli, R. Q. Hood, A. U. Hazi, and F. Gygi, Phys. Rev. B **61**, 909 (2000).

38. L. A. Collins, S. R. Bickham, J. D. Kress, S. Mazevet, T. J. Lenosky, N. J. Troullier, and W. Windl, Phys. Rev. B **63**, 184110 (2001).

39. J. Clérouin and J.-F. Dufrêche, Phys. Rev. E **64**, 066406 (2001).

40. M. P. Desjarlais, Phys. Rev. B **68**, 064204 (2003).

41. S. A. Bonev, B. Militzer, and G. Galli, Phys. Rev. B **69**, 014101 (2004).

42. L. A. Collins, Los Alamos National Laboratory, private communication (2010).

43. F. Lambert, J. Clérouin, and G. Zérah, Phys. Rev. E **73**, 016403 (2006); C. Lambert, J. Clérouin, and S. Mazevet, Europhys. Lett. **75**, 681 (2006); D. A. Horner, F. Lambert, J. D. Kress, and L. A. Collins, Phys. Rev. B **80**, 024305 (2009).

44. B. Militzer, Ph.D. thesis, University of Illinois at Urbana-Champaign, 2000.

45. B. Militzer, Phys. Rev. Lett. **97**, 175501 (2006).

46. B. Militzer, Phys. Rev. B **79**, 155105 (2009).

47. D. M. Ceperley, Rev. Mod. Phys. **67**, 279 (1995).

48. D. M. Ceperley, J. Stat. Phys. **63**, 1237 (1991).

49. D. M. Ceperley, in *Monte Carlo and Molecular Dynamics of Condensed Matter Systems*, edited by K. Binder and G. Ciccotti (Italian Physical Society, Bologna, Italy, 1996).

50. B. Militzer and E. L. Pollock, Phys. Rev. E **61**, 3470 (2000).

51. B. Militzer, W. Magro, and D. Ceperley, Contrib. Plasma Phys. **39**, 151 (2006).

52. P. Debye and E. Hückel, Phys. Z **24**, 185 (1923).

53. D. Keller, T. J. B. Collins, J. A. Delettrez, P. W. McKenty, P. B. Radha, B. Whitney, and G. A. Moses, Bull. Am. Phys. Soc. **44**, 37 (1999); P. B. Radha, T. J. B. Collins, J. A. Delettrez, Y. Elbaz, R. Epstein, V. Y. Glebov, V. N. Goncharov, R. L. Keck, J. P. Knauer, J. A. Marozas, F. J. Marshall, R. L. McCrory, P. W. McKenty, D. D. Meyerhofer, S. P. Regan, T. C. Sangster, W. Seka, D. Shvarts, S. Skupsky, Y. Srebro, and C. Stoeckl, Phys. Plasmas **12**, 056307 (2005); S. X. Hu, V. Smalyuk, V. N. Goncharov, S. Skupsky, T. C. Sangster, D. D. Meyerhofer, and D. Shvarts, Phys. Rev. Lett. **101**, 055002 (2008).

54. T. R. Boehly, D. H. Munro, P. M. Celliers, R. E. Olson, D. G. Hicks, V. N. Goncharov, G. W. Collins, H. F. Robey, S. X. Hu, J. A. Marozas, T. C. Sangster, O. L. Landen, and D. D. Meyerhofer, Phys. Plasmas **16**, 056302 (2009).

55. T. R. Boehly, V. N. Goncharov, W. Seka, M. A. Barrios, P. M. Celliers, D. G. Hicks, G. W. Collins, S. X. Hu, J. A. Marozas, and D. D. Meyerhofer, Phys. Rev. Lett. **106**, 195005 (2011).

56. R. M. More, K. H. Warren, D. A. Young, and G. B. Zimmerman, Phys. Fluids **31**, 3059 (1988).

57. B. A. Remington, S. V. Weber, M. M. Marinak, S. W. Haan, J. D. Kilkenny, R. Wallace, and G. Dimonte, Phys. Rev. Lett. **73**, 545 (1994); H. Azechi, T. Sakaiya, S. Fujioka, Y. Tamari, K. Otani, K. Shigemori, M. Nakai, H. Shiraga, N. Miyanaga, and K. Mima, Phys. Rev. Lett. **98**, 045002 (2007); V. A. Smalyuk, S. X. Hu, V. N. Goncharov, D. D. Meyerhofer, T. C. Sangster, D. Shvarts, C. Stoeckl, B. Yaakobi, J. A. Frenje, and R. D. Petrasso, Phys. Rev. Lett. **101**, 025002 (2008); V. A. Smalyuk, S. X. Hu, V. N. Goncharov, D. D. Meyerhofer, T. C. Sangster, C. Stoeckl, and B. Yaakobi, Phys. Plasmas **15**, 082703 (2008); V. A. Smalyuk, S. X. Hu, J. D. Hager, J. A. Delettrez, D. D. Meyerhofer, T. C. Sangster, and D. Shvarts, Phys. Rev. Lett. **103**, 105001 (2009); V. A. Smalyuk, S. X. Hu, J. D. Hager, J. A. Delettrez, D. D. Meyerhofer, T. C. Sangster, and D. Shvarts, Phys. Plasmas **16**, 112701 (2009).

58. S. X. Hu, P. B. Radha, J. A. Marozas, R. Betti, T. J. B. Collins, R. S. Craxton, J. A. Delettrez, D. H. Edgell, R. Epstein, V. N. Goncharov, I. V. Igumenshchev, F. J. Marshall, R. L. McCrory, D. D. Meyerhofer, S. P. Regan, T. C. Sangster, S. Skupsky, V. A. Smalyuk, Y. Elbaz, and D. Shvarts, Phys. Plasmas **16**, 112706 (2009).

59. S. X. Hu, V. N. Goncharov, P. B. Radha, J. A. Marozas, S. Skupsky, T. R. Boehly, T. C. Sangster, D. D. Meyerhofer, and R. L. McCrory, Phys. Plasmas **17**, 102706 (2010).

60. F. J. Rogers and A. Nayfonov, Astrophys. J. **576**, 1064 (2002).

61. W. Stolzmann and T. Blöcker, Astron. Astrophys. **361**, 1152 (2000).

62. L. Caillabet, S. Mazevet, and P. Loubeyre, Phys. Rev. B **83**, 094101 (2011).

63. L. Caillabet, B. Canaud, G. Salin, S. Mazevet, and P. Loubeyre, Phys. Rev. Lett. **107**, 115004 (2011).

64. M. A. Morales, L. X. Benedict, D. S. Clark, E. Schwegler, I. Tamblyn, S. A. Bonev, A. A. Correa, S. W. Haan, High Energy Density Physics **8**, 5 (2012).

FIGURE CAPTIONS

FIG. 1. (Color online) [(a)–(c)] A cryogenic-DT implosion on OMEGA with the triple-picket step pulse; [(d)–(f)] A direct-drive–ignition design for the NIF, scaled from hydro-equivalent OMEGA implosions. In both cases, strongly coupled and degenerated plasma conditions are indeed accessed.

FIG. 2. (Color online) The temperature and density conditions covered by the FPEOS table. The gray circles represent our PIMC calculations, while the shell conditions in ICF implosions are schematically shown by the region in orange color. The blue and green lines of θ =1 and Γ = 1 characterize the boundaries of degeneracy and coupling conditions, respectively.

FIG. 3. (Color online) The pair-correlation functions $g(r)$ derived from PIMC calculations: (a) the ion–ion correlation $g_{dd}(r)$; (b) the ion–electron correlation $g_{de}(r)$; (c) the electron–electron correlation $g_{eep}(r)$ for parallel spins; (d) the electron–electron correlation $g_{eea}(r)$ for antiparallel spins, with different densities at 15,625 K.

FIG. 4. (Color online) Pair-correlation functions similar to Fig. 3, but at a higher temperature of 2.5×10^5 K and densities from 1.0 to 15.709 g/cm^3.

FIG. 5. (Color online) Pair-correlation functions similar to Fig. 3, but at a higher temperature of 2×10^6 K and densities from 24.945 to 199.56 g/cm^3.

FIG. 6. (Color online) Pair-correlation functions similar to Fig. 3 at a fixed density of 10.0 g/cm^3 for temperatures ranging from 1.25×10^5 K to 2×10^6 K.

FIG. 7. (Color online) The comparisons of (a) pressure and (b) internal energy as a function of density from the FPEOS, *SESAME*, and *Kerley03* tables. The error bars indicate the 1σ statistical uncertainty in the PIMC simulations. Results were normalized to non-interacting gas of classical ions and fermionic electrons.

FIG. 8. (Color online) Same as Fig. 7 but for a different temperature of 2.5×10^5 K. The Debye–Hückel model is also shown for comparison.

FIG. 9. (Color online) Same as Fig. 7 but for a different temperature of 4×10^6 K.

FIG. 10. (Color online) (a) Pressure and (b) energy as a function of temperature from FPEOS, *SESAME*, and *Kerley03* tables for a deuterium density of 0.1 g/cm^3.

FIG. 11. (Color online) Same as Fig. 10 but for a different deuterium density of 1.0 g/cm^3.

FIG. 12. (Color online) Same as Fig. 10 but for a higher deuterium density of 10.0 g/cm^3.

FIG. 13. (Color online) Same as Fig. 10 but for a much higher deuterium density 84.19 g/cm^3.

FIG. 14. (Color online) (a) The triple-picket pulse shape for shock-timing experiments using cryogenic deuterium; (b) the measured shock speed in liquid D_2 (solid black line) compared with hydrodynamic predictions using the *SESAME*, FPEOS, *Kerley03*, and QEOS models.

FIG. 15. (Color online) The hydrocode simulations of a cryogenic-DT implosion on OMEGA using the three different EOS tables including *SESAME*, FPEOS, and *Kerley03*: (a) the laser pulse shape; (b) the density–temperature profiles of the imploding DT shell at the middle of main laser pulse (t = 3.8 ns); (c) the density profile at peak compression (t = 4.26 ns); and (d) the areal density (ρR) and yield as a function of time.

FIG. 16. (Color online) Similar to Fig. 15 but for a hydroequivalent, direct-drive, 1-MJ ignition design for the NIF.

FIG. 17. (Color online) The density contour plots at t = 3.85 ns from 2-D *DRACO* simulations of the OMEGA cryogenic-DT implosion shown in Fig. 15, respectively, using the (a) *SESAME* and (b) FPEOS for the fuel DT. It is noted that the various perturbation sources have been included up to mode ℓ = 150.

FIG. 18. (Color online) (a) The modal spectrum of perturbation amplitude at the ablation surface for t . 3.0 ns (the beginning of acceleration); (b) the perturbation growth in ρR as a function of time, analyzed from the 2-D *DRACO* simulations shown in Fig. 17.

TABLES

TABLE I: FPEOS table with pressures and internal energy per atom for deuterium. The statistical uncertainties from the PIMC simulations are given in brackets e.g., 0.219(5) = 0.219±0.005, 414.4(1.6) = 414.4±1.6, or 70230(400) = 70230±400.

Temperature (K)	Pressure (Mbar)	Internal energy (eV/atom)
	$\rho = 1.96360 \times 10^{-3}$ g/cm^3 [r_s = 14.0 Bohr]	
15,625	0.001290(8)	–10.83(3)
31,250	0.003364(8)	–2.867(16)
62,500	0.009046(8)	11.930(13)
95,250	0.014640(8)	21.870(12)
125,000	0.019600(10)	30.080(15)
181,825	0.028920(8)	45.190(13)
250,000	0.40040(12)	63.04(2)
400,000	0.06440(2)	102.00(4)
500,000	0.08074(2)	128.10(4)
1,000,000	0.16170(3)	257.30(6)
2,000,000	0.323290(6)	515.90(10)
4,000,000	0.64830(14)	1033.0(2)
	$\rho = 3.11810 \times 10^{-3}$ g/cm^3 [r_s = 12.0 Bohr]	
15,625	0.002048(14)	–10.97(3)
31,250	0.005105(14)	–3.82(2)
62,500	0.013980(12)	10.860(12)
95,250	0.022970(11)	21.180(12)
125,000	0.030840(15)	29.490(15)
181,825	0.045690(13)	44.720(13)
250,000	0.063400(19)	62.67(2)
400,000	0.10220(4)	101.80(4)
500,000	0.12790(3)	127.70(4)
1,000,000	0.25670(5)	257.10(5)
2,000,000	0.51440(10)	516.00(10)
4,000,000	1.0290(2)	1033.0(2)

	$\rho = 5.38815 \times 10^{-3}$ g/cm^3 [r_s = 10.0 Bohr]	
15,625	0.00349(2)	–11.280(20)
31,250	0.00845(2)	–4.841(18)
62,500	0.02325(2)	9.401(14)
95,250	0.038870(19)	20.080(12)
125,000	0.05264(3)	28.620(16)
181,825	0.07841(2)	44.040(13)
250,000	0.10900(3)	62.090(19)
400,000	0.17630(7)	101.40(4)
500,000	0.22080(7)	127.30(4)
1,000,000	0.44360(9)	257.00(5)
2,000,000	0.88830(19)	515.50(11)
4,000,000	1.7780(4)	1033.0(2)
	$\rho = 1.05237 \times 10^{-2}$ g/cm^3 [r_s = 8.0 Bohr]	
15,625	0.00659(5)	–11.550(17)
31,250	0.01580(6)	–5.860(20)
62,500	0.04325(4)	7.477(13)
95,250	0.07371(4)	18.450(12)
125,000	0.10080(5)	27.220(16)
181,825	0.15150(4)	42.940(13)
250,000	0.21160(7)	61.18(2)
400,000	0.34300(7)	61.18(2)
500,000	0.43010(13)	126.70(4)
1,000,000	0.86550(19)	256.50(6)
2,000,000	1.7350(4)	515.40(4)
4,000,000	3.4740(8)	1.033.0(2)

TABLE II: TABLE I (Continued).

Temperature (K)	Pressure (Mbar)	Internal energy (eV/atom)
	$\rho = 2.49451 \times 10^{-2}$ g/cm^3 [r_s = 6.0 Bohr]	
15,625	0.01485(12)	–11.820(17)
31,250	0.03556(11)	–6.948(13)
62,500	0.09550(10)	4.773(12)
95,250	0.16610(10)	15.740(13)
125,000	0.23050(11)	24.790(14)
181,825	0.35170(12)	40.920(16)
250,000	0.4946(2)	59.40(3)
400,000	0.8072(4)	99.19(5)
500,000	1.0150(3)	125.40(4)
1,000,000	2.0480(5)	255.50(6)
2,000,000	4.1090(9)	514.50(12)
4,000,000	8.2310(17)	1032.0(2)
	$\rho = 4.31052 \times 10^{-2}$ g/cm^3 [r_s = 5.0 Bohr]	
15,625	0.02537(20)	–11.970(16)
31,250	0.05980(19)	–7.537(14)
62,500	0.15800(16)	3.087(12)
95,250	0.27800(18)	13.820(13)
125,000	0.3880(3)	22.910(18)
181,825	0.5976(2)	39.250(17)
250,000	0.8460(3)	58.01(3)
400,000	1.3870(4)	97.96(3)
500,000	1.7460(5)	124.40(4)
1,000,000	3.5310(8)	254.50(6)
2,000,000	7.0960(13)	513.80(10)
4,000,000	14.220(3)	1031.0(2)
	$\rho = 8.41898 \times 10^{-2}$ g/cm^3 [r_s = 4.0 Bohr]	
15,625	0.0479(7)	–12.21(2)
31,250	0.1150(5)	–8.135(19)

62,500	0.20950(6)	1.17(2)
95,250	0.5200(6)	11.37(2)
125,000	0.7308(7)	20.29(3)
181,825	1.1400(6)	36.80(2)
250,000	1.6250(9)	55.71(3)
400,000	2.6850(11)	96.11(4)
500,000	3.3910(11)	122.70(4)
1,000,000	6.8810(15)	253.30(6)
2,000,000	13.850(3)	513.00(11)
4,000,000	27.750(6)	1030.0(2)
	$\rho = 0.1$ g/cm^3 [r_s . 3.777 Bohr]	
15,625	0.0578(15)	–12.21(5)
31,250	0.1351(6)	–8.351(19)
62,500	0.3491(6)	0.74(2)
95,250	0.6110(6)	10.690(18)
125,000	0.8598(8)	19.57(2)
181,825	1.3450(9)	36.08(3)
250,000	1.9200(9)	55.00(3)
400,000	3.1850(13)	95.67(4)
500,000	4.0180(11)	122.10(4)
1,000,000	8.1680(17)	252.90(5)
2,000,000	16.440(3)	512.40(11)
4,000,000	32.970(7)	1030.0(2)

TABLE III: TABLE I (Continued).

Temperature (K)	Pressure (Mbar)	Internal energy (eV/atom)
	ρ = 0.199561 g/cm^3 [r_s = 3.0 Bohr]	
15,625	0.124(3)	–12.31(4)
31,250	0.2740(17)	–8.91(3)
62,500	0.6730(17)	–1.11(3)
95,250	1.760(16)	8.14(3)
125,000	1.656(2)	16.66(3)
181,825	2.6060(15)	32.91(2)
250,000	3.753(2)	51.98(3)
400,000	6.273(3)	92.85(4)
500,000	7.943(2)	119.60(4)
1,000,000	16.250(5)	251.10(8)
2,000,000	32.760(7)	510.90(11)
4,000,000	65.740(14)	1029.0(2)
	ρ = 0.306563 g/cm^3 [r_s = 2.6 Bohr]	
15,625	0.219(5)	–12.29(5)
31,250	0.447(4)	–9.15(4)
62,500	1.1048(4)	–1.90(4)
95,250	1.781(5)	6.68(5)
125,000	2.509(4)	14.98(4)
181,825	3.947(3)	30.97(4)
250,000	5.693(5)	49.91(5)
400,000	9.558(8)	90.87(8)
500,000	12.120(6)	117.70(6)
1,000,000	24.890(9)	249.60(9)
2,000,000	50.250(13)	509.70(13)
4,000,000	101.100(19)	1030.0(2)
	ρ = 0.389768 g/cm^3 [r_s = 2.4 Bohr]	
15,625	0.298(12)	–12.30(10)
31,250	0.597(9)	–9.21(7)
62,500	1.337(8)	–2.40(7)
95,250	2.280(7)	6.11(6)

125,000	3.175(8)	14.09(7)
181,825	4.979(11)	29.84(9)
250,000	7.206(9)	48.84(7)
400,000	12.090(12)	89.61(9)
500,000	15.370(14)	116.70(11)
1,000,000	31.580(14)	248.60(11)
2,000,000	63.96(2)	509.80(19)
4,000,000	128.40(3)	1028.0(3)
	$\rho = 0.506024$ g/cm^3 [$r_s = 2.2$ Bohr]	
15,625	0.42(3)	–12.1(2)
31,250	0.849(14)	–9.16(9)
62,500	1.789(12)	–2.68(7)
95,250	2.954(10)	5.30(6)
125,000	4.088(12)	13.02(7)
181,825	6.396(10)	28.48(6)
250,000	9.243(12)	47.20(7)
400,000	15.620(14)	88.25(9)
500,000	19.84(3)	115.10(18)
1,000,000	40.94(3)	247.5(2)
2,000,000	82.93(3)	508.6(2)
4,000,000	166.50(4)	1026.0(3)

TABLE IV: TABLE I (Continued).

Temperature (K)	Pressure (Mbar)	Internal energy (eV/atom)
	ρ = 0.673518 g/cm^3 [r_s = 2.0 Bohr]	
15,625	0.59(4)	–12.02(18)
31,250	1.28(2)	–8.96(11)
62,500	2.461(10)	–3.01(5)
95,250	3.930(7)	4.43(3)
125,000	5.413(6)	11.91(3)
181,825	8.446(8)	27.08(4)
250,000	12.200(7)	45.63(3)
400,000	20.660(14)	86.64(6)
500,000	26.270(15)	113.50(7)
1,000,000	54.300(20)	245.90(9)
2,000,000	110.20(3)	507.20(16)
4,000,000	221.60(6)	1026.03(3)
	ρ = 0.837338 g/cm^3 [r_s = 1.86 Bohr]	
15,625	0.97(6)	–11.3(2)
31,250	1.71(2)	–8.85(8)
62,500	3.17(4)	–3.17(14)
95,250	5.04(4)	4.30(14)
125,000	6.80(3)	11.43(11)
181,825	10.52(2)	26.29(9)
250,000	15.15(3)	44.67(10)
400,000	25.62(4)	85.52(16)
500,000	32.67(4)	112.70(17)
1,000,000	67.44(6)	244.9(2)
2,000,000	136.90(11)	506.2(4)
4,000,000	275.50(8)	1026.0(3)
	ρ = 1.0 g/cm^3 [r_s = 1.753 Bohr]	
15,625	1.33(7)	–11.0(2)
31,250	2.22(4)	–8.67(12)
62,500	3.92(4)	–3.23(14)
95,250	6.06(4)	3.88(13)

125,000	8.16(4)	10.90(11)
181,825	12.57(3)	25.60(10)
250,000	18.07(3)	43.85(10)
400,000	30.36(3)	84.00(9)
500,000	38.81(3)	111.30(10)
1,000,000	80.40(4)	243.90(13)
2,000,000	163.20(6)	505.00(17)
4,000,000	328.80(8)	1024.0(3)
	$\rho = 1.00537$ g/cm^3 [$r_s = 1.750$ Bohr]	
15,625	1.35(9)	–10.9(3)
31,250	2.23(3)	–8.69(10)
62,500	4.03(4)	–2.97(14)
95,250	6.03(5)	3.67(16)
125,000	8.27(5)	11.09(14)
181,825	12.63(3)	25.56(9)
250,000	18.17(4)	43.82(13)
400,000	30.54(5)	84.05(16)
500,000	38.99(8)	111.2(3)
1,000,000	80.80(7)	243.7(2)
2,000,000	164.20(11)	505.3(3)
4,000,000	330.50(12)	1024.0(4)

TABLE V: TABLE I (Continued).

Temperature (K)	Pressure (Mbar)	Internal energy (eV/atom)
	ρ = 1.15688 g/cm^3 [r_s = 1.67 Bohr]	
15,625	1.67(11)	–10.93(3)
31,250	2.78(5)	–8.35(14)
62,500	4.82(6)	–2.87(16)
95,250	7.05(6)	3.49(17)
125,000	9.65(6)	10.93(17)
181,825	14.45(6)	24.77(17)
250,000	20.81(5)	42.94(14)
400,000	35.12(5)	83.36(13)
500,000	44.82(3)	110.50(9)
1,000,000	92.99(5)	243.30(13)
2,000,000	189.00(11)	505.0(3)
4,000,000	380.30(16)	1024.0(4)
	ρ = 1.31547 g/cm^3 [r_s = 1.60 Bohr]	
31,250	3.46(9)	–7..9(2)
62,500	5.65(10)	–2.8(2)
95,250	8.31(8)	3.75(19)
125,000	10.97(6)	10.44(15)
181,825	16.66(6)	24.76(14)
250,000	23.73(5)	42.50(12)
400,000	39.92(7)	82.72(17)
500,000	50.66(7)	109.20(17)
1,000,000	105.50(8)	242.30(20)
2,000,000	214.20(7)	502.90(16)
4,000,000	431.80(11)	1022.0(3)
	ρ = 1.59649 g/cm^3 [r_s = 1.50 Bohr]	
31,250	4.67(13)	–7.5(3)
62,500	7.24(13)	–2.7(2)
95,250	10.53(13)	3.9(2)
125,000	13.68(11)	10.4(2)
181,825	20.19(7)	23.87(13)

250,000	28.78(8)	41.57(15)
400,000	48.31(7)	81.53(14)
500,000	61.33(10)	107.90(19)
1,000,000	128.20(11)	241.8(2)
2,000,000	260.40(15)	503.1(3)
4,000,000	524.30(13)	1022.0(3)
	$\rho = 1.96361$ g/cm^3 [$r_s = 1.40$ Bohr]	
31,250	6.4(2)	–7.0(4)
62,500	9.69(15)	–2.1(2)
95,250	13.66(14)	4.3(2)
125,000	17.11(10)	10.05(16)
181,825	25.29(6)	23.68(9)
250,000	35.66(9)	41.00(14)
400,000	59.23(9)	80.18(15)
500,000	75.41(10)	106.90(15)
1,000,000	156.80(9)	239.50(15)
2,000,000	319.49(16)	501.2(3)
4,000,000	644.54(18)	1021.0(3)

TABLE VI: TABLE I (Continued).

Temperature (K)	Pressure (Mbar)	Internal energy (eV/atom)
	ρ = 2.45250 g/cm^3 [r_s = 1.30 Bohr]	
62,500	12.61(7)	–2.2(2)
95,250	18.18(16)	4.9(2)
125,000	22.09(15)	1005(19)
181,825	32.63(10)	24.00(13)
250,000	45.03(12)	40.55(15)
400,000	74.54(10)	79.73(13)
500,000	93.88(11)	105.30(14)
1,000,000	195.60(17)	238.1(2)
2,000,000	398.20(18)	499.41(2)
4,000,000	804.2(3)	1020.4(4)
	ρ = 3.11814 g/cm^3 [r_s = 1.20 Bohr]	
62,500	18.0(4)	–1.4(4)
95,250	4.6(3)	5.4(4)
125,000	30.1(5)	11.0(5)
181,825	43.0(3)	24.4(4)
250,000	57.8(4)	39.9(4)
400,000	94.9(2)	78.5(2)
500,000	120.10(14)	104.70(14)
1,000,000	248.4(2)	236.7(3)
2,000,000	504.5(6)	496.7(6)
4,000,000	1021.0(5)	1018.0(5)
	ρ = 4.04819 g/cm^3 [r_s = 1.10 Bohr]	
62,500	26.2(1.1)	–0.1(8)
95,250	34.4(5)	6.1(4)
125,000	41.9(6)	12.1(5)
181,825	58.8(6)	25.3(5)
250,000	75.8(4)	39.0(3)
400,000	125.1(3)	78.5(2)
500,000	156.8(2)	103.80(16)
1,000,000	321.0(3)	234.0(3)

2,000,000	651.5(7)	492.9(5)
4,000,000	1327.0(8)	1018.0(6)
	ρ = 5.38815 g/cm^3 [r_s = 1.00 Bohr]	
95,250	51.9(1.6)	8.3(9)
125,000	61.1(8)	13.7(5)
181,825	81.8(1.2)	25.9(7)
250,000	105.4(8)	40.0(5)
400,000	169.1(1.3)	78.2(7)
500,000	212.2(1.3)	104.1(8)
1,000,000	429.4(1.1)	233.5(6)
2,000,000	867.4(1.2)	491.5(7)
4,000,000	1768.0(1.0)	1018.0(6)
	ρ = 17.39115 g/cm^3 [r_s = 0.90 Bohr]	
95,250	80(2)	10.3(9)
125,000	92(2)	15.5(9)
181,825	120(2)	27.4(1.0)
250,000	153.4(1.3)	41.9(6)
400,000	236.6(1.5)	78.2(6)
500,000	297.2(1.2)	104.5(5)
1,000,000	590.2(1.4)	231.8(6)
2,000,000	1183.0(1.6)	486.5(7)
4,000,000	2422.0(1.6)	1015.0(7)

TABLE VII: TABLE I (Continued).

Temperature (K)	Pressure (Mbar)	Internal energy (eV/atom)
	ρ = 10.0000 g/cm^3 [r_s . 0.81373 Bohr]	
125,000	142(3)	19.0(8)
181,825	182(2)	31.8(7)
250,000	225.7(1.7)	44.5(5)
400,000	334(4)	80.5(1.3)
500,000	414.4(1.6)	106.2(5)
1,000,000	802(2)	230.5(6)
2,000,000	1596.0(1.6)	483.3(5)
4,000,000	3276.0(1.6)	1013.0(5)
8,000,000	6592(3)	2054.0(8)
	ρ = 10.5237 g/cm^3 [r_s = 0.80 Bohr]	
125,000	153(7)	19.8(2.0)
181,825	197(4)	33.1(1.0)
250,000	242(3)	45.4(9)
400,000	353(4)	80.4(1.2)
500,000	434(4)	105.3(1.1)
1,000,000	846(3)	231.0(8)
2,000,000	1681(2)	283.2(7)
4,000,000	3447(6)	1011.0(1.8)
8,000,000	6929(3)	2051.0(9)
	ρ = 15.7089 g/cm^3 [r_s = 1.70 Bohr]	
181,825	346(9)	40.0(1.7)
250,000	419(9)	55.01(1.8)
400,000	575(4)	87.1(8)
500,000	684(3)	109.3(6)
1,000,000	1293(4)	233.5(7)
2,000,000	2515(4)	481.04(9)
4,000,000	5149(5)	1011.0(1.1)
8,000,000	10390(5)	2060.0(1.1)

	ρ = 24.9451 g/cm^3 [r_s = 0.60 Bohr]	
400,000	1037(12)	98.4(1.4)
500,000	1208(17)	121(2)
1,000,000	2133(11)	239.21(1.4)
2,000,000	4025(9)	480.9(1.1)
4,000,000	8195(16)	1009.0(2.0)
8,000,000	16200(17)	2020(2)
16,000,000	32950(13)	4124.0(1.6)
	ρ = 43.1052 g/cm^3 [r_s = 0.50 Bohr]	
400,000	2212(30)	123(2)
500,000	2523(20)	146.5(1.8)
1,000,000	4002(30)	256.4(2.0)
2,000,000	7162(18)	490.2(1.3)
4,000,000	14180(17)	1006.0(1.3)
8,000,000	28390(30)	2044(2)
16,000,000	56880(20)	4118.0(1.7)
32,000,000	114000(40)	8273(3)
64,000,000	227900(90)	16540(7)
	ρ = 84.1898 g/cm^3 [r_s = 0.40 Bohr]	
1,000,000	9169(50)	298.4(2.0)
2,000,000	14950(80)	517(3)
4,000,000	27960(70)	1007(3)
8,000,000	54980(40)	2019.0(1.4)
16,000,000	110600(70)	4093(3)
32,000,000	222600(120)	8262(4)
64,000,000	445900(110)	16570(4)

TABLE VIII: TABLE I (Continued).

Temperature (K)	Pressure (Mbar)	Internal energy (eV/atom)
	ρ = 199.561 g/cm^3 [r_s = 0.30 Bohr]	
2,000,000	41350(800)	597(12)
4,000,000	70230(400)	1056(6)
8,000,000	129900(500)	2000(8)
16,000,000	263400(300)	4104(5)
32,000,000	527000(400)	8247(7)
64,000,000	1049000(400)	16450(7)
	ρ = 673.518 g/cm^3 [r_s = 0.20 Bohr]	
4,000,000	299900(4000)	1322(16)
8,000,000	504200(3000)	2281(15)
16,000,000	897500(1300)	4121(6)
32,000,000	1783000(1700)	8251(8)
64,000,000	3569000(1600)	16560(7)
	ρ = 1596.49 g/cm^3 [r_s = 0.15 Bohr]	
4,000,000	1071000(20000)	2002(40)
8,000,000	1555000(20000)	29631(40)
16,000,000	2342000(17000)	4517(30)
32,000,000	4565000(16000)	8890(30)
64,000,000	8523000(8000)	16670(17)

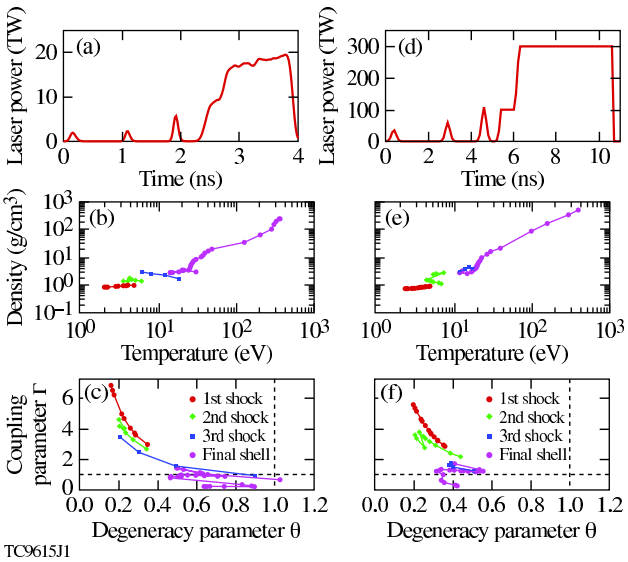

Figure 1 BJ12034 21NOV2011

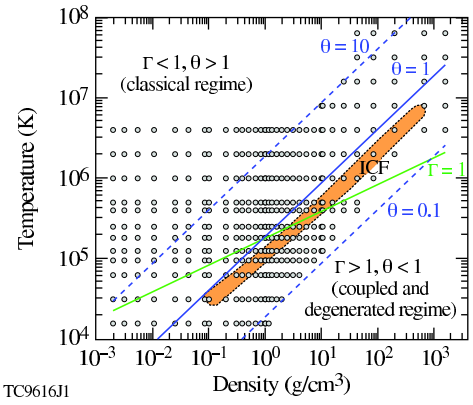

Figure 2 BJ12034 21NOV2011

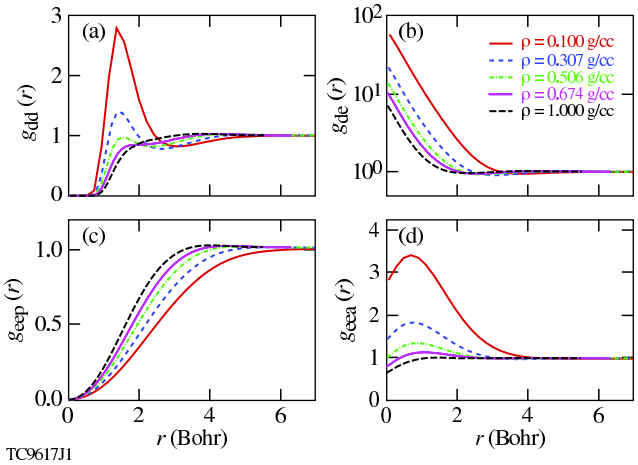

Figure 3 BJ12034 21NOV2011

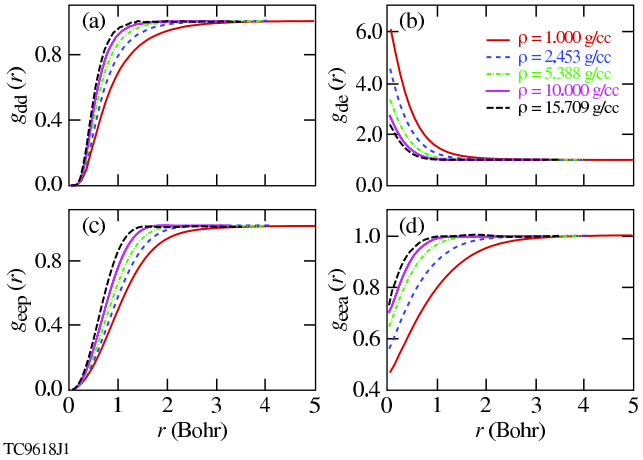

Figure 4 BJ12034 21NOV2011

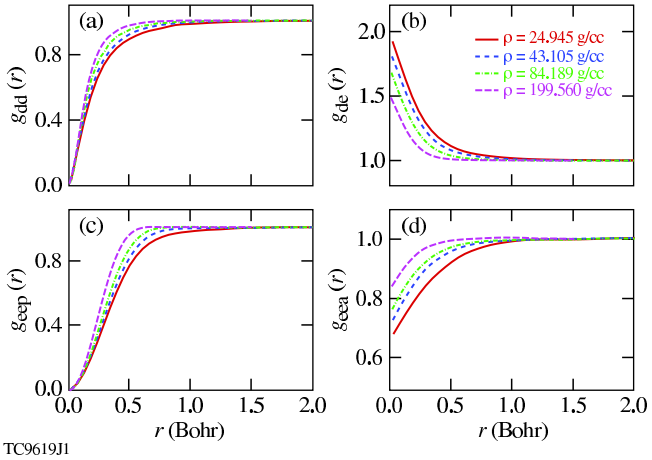

Figure 5 BJ12034 21NOV2011

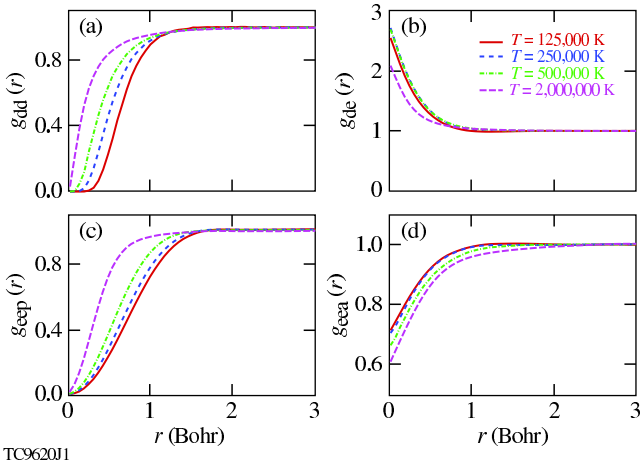

Figure 6 BJ12034 21NOV2011

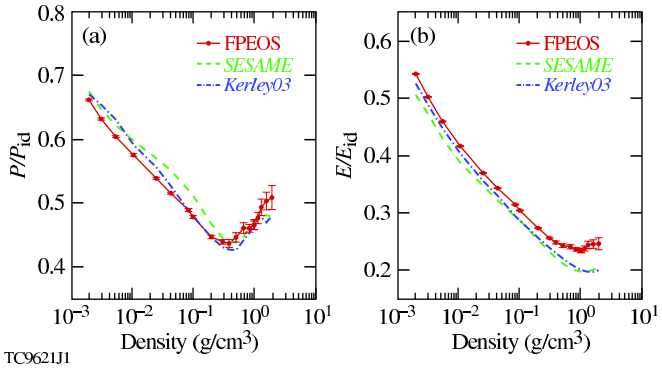

Figure 7 BJ12034 21NOV2011

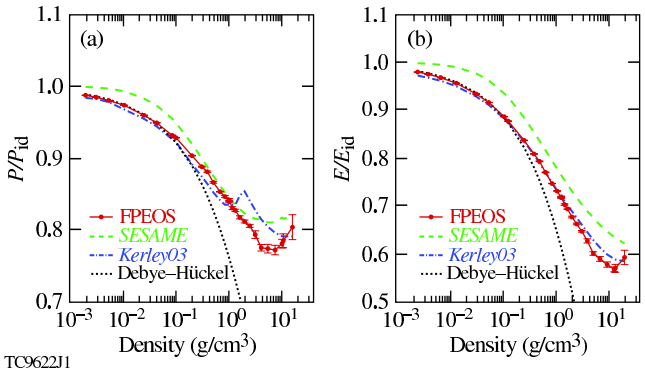

Figure 8 BJ12034 21NOV2011

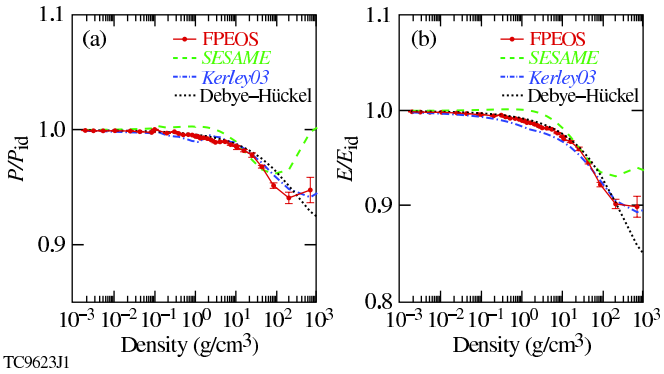

Figure 9 BJ12034 21NOV2011

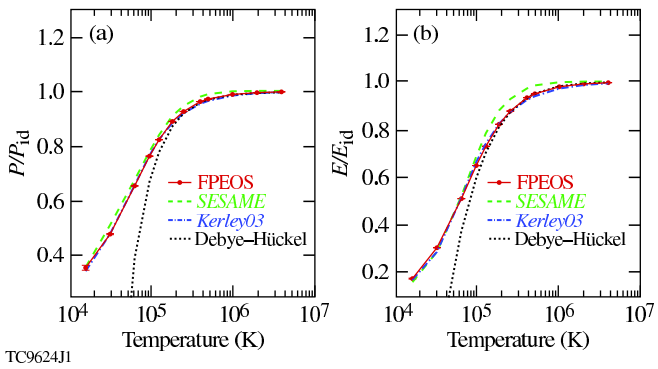

Figure 10 BJ12034 21NOV2011

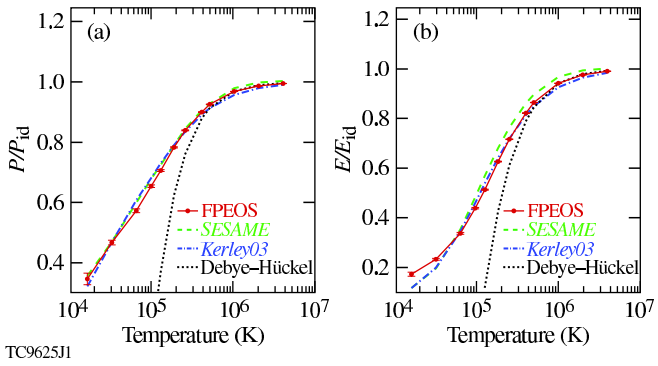

Figure 11 BJ12034 21NOV2011

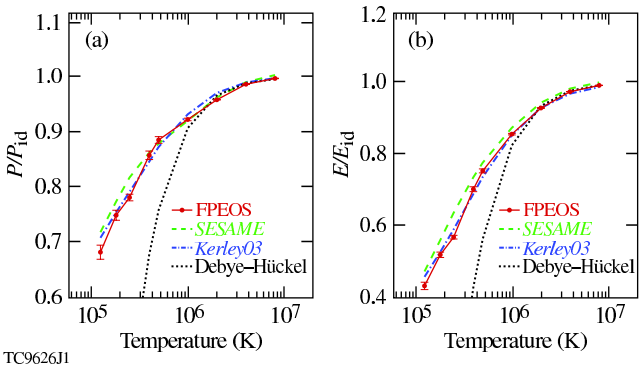

Figure 12 BJ12034 21NOV2011

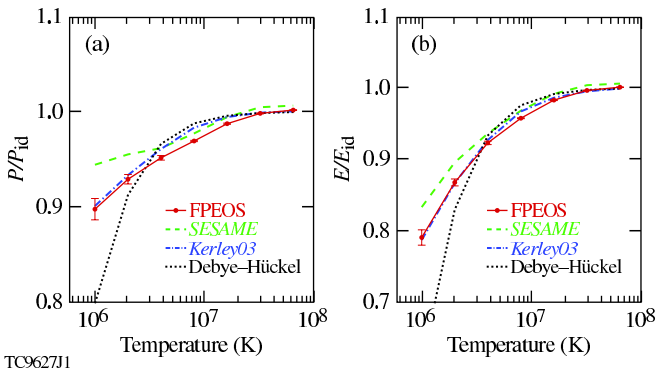

Figure 13 BJ12034 21NOV2011

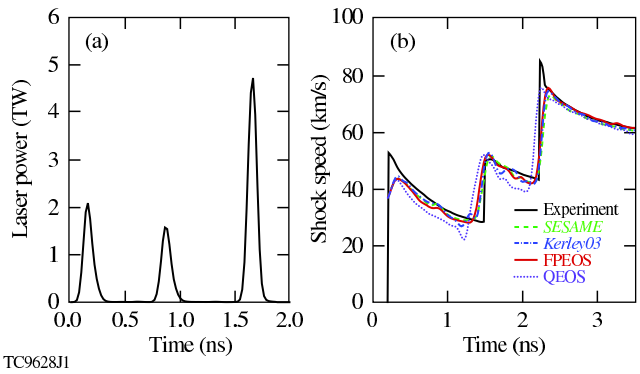

Figure 14 BJ12034 21NOV2011

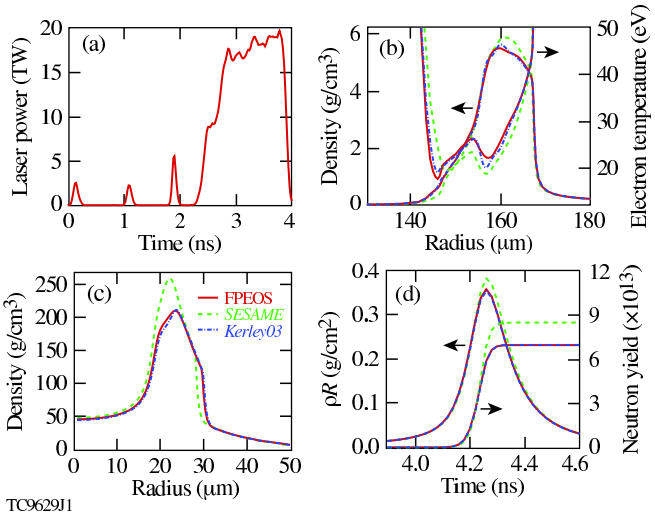

Figure 15 BJ12034 21NOV2011

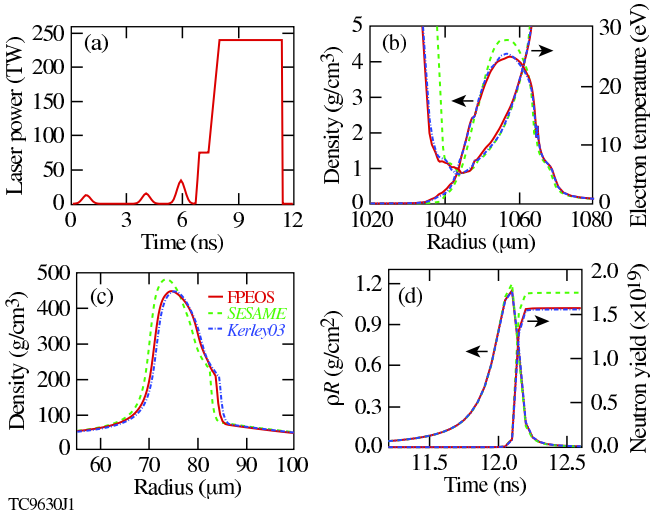

Figure 16 BJ12034 21NOV2011

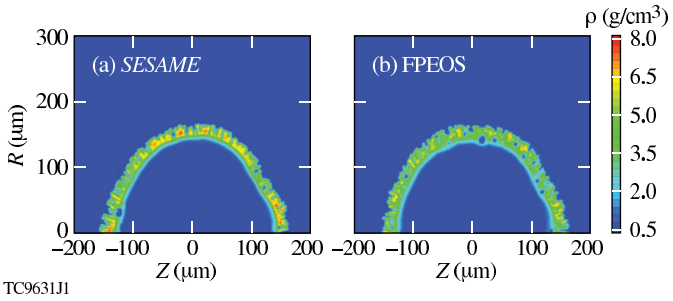

Figure 17 BJ12034 21NOV2011

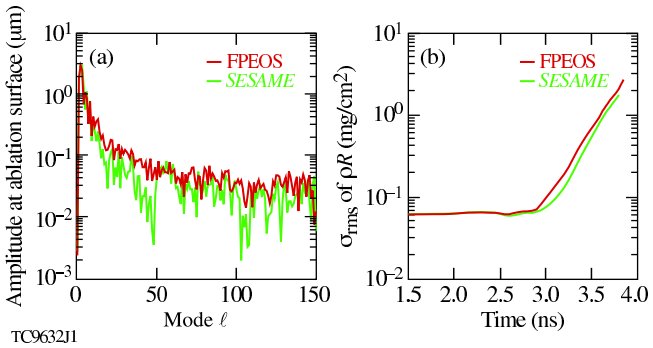

Figure 18 BJ12034 21NOV2011